THE ASTROPHYSICAL JOURNAL, 271:143–160, 1983 August 1

A GRAVITATIONALLY STABLE BOK GLOBULE

R. L. DICKMAN AND DAN P. CLEMENS
Five College Radio Astronomy Observatory; and Department of Physics and Astronomy, University of Massachusetts
Received 1982 September 13; accepted 1983 January 20

ABSTRACT

A molecular and optical study of an isolated, low-mass ($\sim 10\ M_\odot$) Bok globule is presented. Analysis of the cloud's surface brightness reveals the object to be centrally condensed. Molecular emission lines are unusually narrow, implying that any turbulent motions within the cloud are subsonic. Consequently, thermal pressure dominates dynamical support by a wide margin within the globule. A stability assessment based upon the cloud properties obtained from the observations suggests that the cloud is close to a state of hydrostatic equilibrium. Owing to the relatively insignificant role played by turbulent pressure in supporting the globule, stable cloud configurations can be modeled with some confidence. A pressure-bounded, centrally condensed model with kinetic temperature increasing outward yields good agreement with the observed cloud radius and central visual extinction, as well as with the mass inferred from the observations. Neither the requirement of equilibrium nor the slight ellipticity of the cloud appears to demand ad hoc postulation of a significant internal magnetic field. The hydrostatic models are also used to construct microturbulent CO line formation models of the globule; these agree well with the observations.

Subject headings: interstellar: molecules — nebulae: general

I. INTRODUCTION

Bok globules are the simplest unit structures in the dense interstellar medium. Their high degree of geometrical regularity and lack of strong internal energy sources make them ideal subjects for a comparison of observation and theory. Radio and optical data for a particular cloud can, in principle, provide a sufficiently complete portrait of its mass distribution, temperature, size, and dynamical state, so that theoretical ideas regarding the behavior of a reasonably spherical system under the action of self-gravitation can be explored and refined.

In practice, this is difficult to do. While observations of trace molecules such as CO have unequivocally established the presence of large-amplitude and usually supersonic bulk motions within globules, the character of these flows is not easily extracted from the data. If predominantly ordered, their presence implies large-scale expansion or contraction. If, instead, the flow possesses a significant turbulent component, the associated dynamical stress allows for a great variety of possible kinematic states, dramatically altering the picture one has of the cloud.

Without observational tests to discriminate between these two scenarios, detailed comparison between observation and theory are difficult. In effect, the dynamical state of the cloud, which should follow from observation, is generally a precondition *for* the construction of a detailed model. A very wide range of dynamical states must then be considered in order to establish a reasonably conclusive correspondence between observations and a particular model. Further, if as is usually the case, observations suggest that turbulence in a given cloud may be supersonic, hydrodynamic model states become exceedingly difficult to specify with any precision. At best one is faced with a formidable, if not hopeless, task.

This paper reports results of a comprehensive radio and optical study of a Bok globule for which these difficulties are largely absent. This simplification is possible because the molecular lines emitted by the globule are extremely narrow. If one chooses to interpret the observed line widths in terms of turbulent internal motions, one finds the entire cloud to be subsonic. This implies that thermal pressure within the globule dominates dynamical support by *at least* a factor of 10, so that equilibrium configurations are easily modeled. When compared with collapse or expansion models, the equilibrium case fares so well that it is difficult to avoid the conclusion that the system is stable. Ramifications of this are discussed both as they apply to the formation and evolution of this cloud, as well as for the more general population of dark globules.

II. RADIO OBSERVATIONS AND PHOTOMETRIC DATA

The observational data for this study consist of spectral-line data at both 3 and 1 mm wavelengths, in addition to densitometric measurements of the cloud's surface brightness from the Palomar Observatory Sky Survey (POSS) prints. Details of the data acquisition are provided below.

a) 3 mm *Spectral-Line Data*

Observations of the $J = 1 \rightarrow 0$ lines of $^{12}C^{16}O$, $^{13}C^{16}O$, and $^{12}C^{18}O$ (hereafter denoted CO, ^{13}CO, $C^{18}O$) were made during winter 1980–1981 using the 14 m antenna of the Five College Radio Astronomy

Observatory (FCRAO).[1] At 2.6 mm the 14 m antenna had a measured half-power beamwidth (HPBW) of 47″ and a main beam efficiency of about 40%, including radome loss. The cooled 80–120 GHz Schottky receiver had a single-sideband noise temperature of 450–500 K measured at the input of the quasi-optical single-sideband filter. Antenna pointing—a critical factor given the small size of the cloud—was repeatedly verified to be good to better than 7″, rms. Data were calibrated by means of an ambient-temperature chopper wheel (Penzias and Burrus 1973), using a scheme which accounts for the effects of the antenna radome. Baseline stability was achieved by frequency-switching the local oscillator at 5 Hz over a separation chosen to place the CO lines symmetrically within the bandpass of the 256 channel autocorrelator back end. A total correlator bandwidth of 10 MHz was usually employed, providing a channel separation of 0.10 km s^{-1} at the CO line frequency; a correlator bandwidth of 5 MHz was used to observe the extremely narrow $C^{18}O$ lines. All frequency-switched spectra were subsequently folded to enhance their signal-to-noise ratio.

b) 1 mm *Spectral-Line Data*

CO and ^{13}CO spectra of the $J = 2 \rightarrow 1$ lines were also obtained toward the center of the globule in the spring of 1981, using an FCRAO cooled Schottky receiver (Erickson 1981) installed on the 4.9 m antenna of the Millimeter Wave Observatory (MWO).[2] At 1.3 mm the antenna has a HPBW of 1′.3 and a main beam efficiency of about 50%. The receiver had a single-sideband noise temperature of about 900 K; although no image sideband rejection filter was employed, laboratory tests demonstrated that the receiver gains in both sidebands were essentially identical (Erickson, private communication). Antenna pointing was found to be reproducible to about 20″. Spectral-line calibration was achieved with a chopper vane. While ^{13}CO data were obtained by frequency-switching at 5 Hz, at the time of the observations the telluric CO line lay too close in frequency to the globule emission to allow the use of frequency-switching; consequently, data for this species were obtained by position-switching the antenna. All MWO data were obtained with a 128 × 62.5 KHz filter bank, which afforded a channel resolution of 0.08 km s^{-1} at 230 GHz.

c) *Densitometry*

In order to analyze the density structure of the cloud, surface brightness profiles of the globule were obtained in blue and red colors. Photographic negatives of both the O and E POSS prints of the globule region were made at an enlarged scale of 21.″5 mm^{-1}. Major and minor axis tracings of emulsion density versus position were then obtained with a microdensitometer using slit dimensions 0.02 × 0.06 mm, with the smaller value corresponding to the trace direction. Interpretation of the photometric data is discussed in § III*b*(ii).

III. OBSERVATIONAL RESULTS

a) *Basic Data*

The globule lies in Cassiopeia, its geometrical center being located at $\alpha(1950) = 0^h36^m17^s.0$, $\delta(1950) = 52°34'37''$; in galactic coordinates $l = 121.04$, $b = -9°.95$. The cloud is extremely well isolated from other dark material in this region, which is very sparse. The nearest dark cloud is the Lynds 1295-1296 complex, which is located about 1° SE of the globule and which differs in CO radial velocity by less than 0.5 km s^{-1} from its neighbor. A distance of 600 pc has been assigned to the globule as discussed in Appendix A.

Figure 1 (Plate 5) is an enlargement of the Palomar Sky Survey (POSS) blue image of the globule. The cloud is distinctly elliptical and consists of an opaque dark core encircled by a bright rim. The rim is produced by anisotropic dust grain scattering of starlight and the diffuse galactic light (DGL, § III*b*[ii]). The size of the opaque core is approximately 1′.2 × 1′.7, corresponding to a mean core radius of 0.12 pc at the adopted distance of 600 pc. Although the extent of the diffuse bright rim is more difficult to establish, the surface brightness photometry suggests half-power outer dimensions of approximately 4′ × 3′, with a mean half-power rim thickness of ~1′.

b) *Optical*

i) *Core Extinction*

The region of the globule interior to the bright rim (cf. Fig. 1) appears totally opaque on the POSS blue print. However, three stellar images, just at the emulsion limit, are discernible within the core on the red print. The mean visual extinction of the core, $\langle A_v \rangle$, can then be inferred by standard star count methods (Dickman 1978*a*), which lead to

$$\langle A_v \rangle = 1.85^{+1.35}_{-0.74} \text{ mag}, \quad (1)$$

where the formal error has been assigned on the basis of a $N^{1/2}$ uncertainty in the counts for the core.

ii) *Surface Brightness*

Quantitative analysis of the globule's bright rim (Fig. 1) is useful in at least two respects. First, it provides a cross-check on the core extinction deduced via star counts. Second, assuming dust and gas in the cloud to be well mixed, it provides a valuable guide to the extent and nature of density variations with position; while an analysis of extinction variations across the cloud can in principle also provide this information (Bok 1956; Schmidt 1975), the globule is far too small and star count uncertainties too large to make the method practical.

[1] The Five College Radio Astronomy Observatory is operated with support from the National Science Foundation under grant AST 81-21481 and with permission of the Metropolitan District Commision, Commonwealth of Massachusetts.

[2] The Millimeter Wave Observatory is operated by the Electrical Engineering Research Laboratory of the University of Texas at Austin with support from the National Science Foundation and McDonald Observatory.

Monte Carlo simulations of the radiation scattering problem in dust clouds have been considered, for example, by Matilla (1970*a*, *b*) and Witt and Stephens (1974, hereafter WS). The latter study is particularly significant since it demonstrates that the presence of a strong density gradient in a cloud is unambiguously recapitulated in the behavior of its rim brightness. This work was subsequently extended and applied by FitzGerald, Stephens, and Witt (1976, FSW) to the Thumbprint Nebula, a bright-rimmed globule morphologically similar to the present cloud.

The results given by WS and FSW can be summarized as follows. For uniform, isotropic illumination—a reasonable assumption for clouds within 150 pc of the galactic plane, since both the stellar and dust grain density responsible for the DGL have scale heights near this value (Witt 1968)—WS determine surface brightness distributions for clouds having a wide range of albedo, scattering asymmetry, and optical depth. Clouds of both uniform and r^{-2} density are considered. The uniform density models appropriate to small globules (having total core optical depths of 2–8) exhibit wide, uniformly dark cores and thin bright rims, the relative rim thickness to cloud radius typically being $W/R \sim 0.1$. By contrast, centrally condensed models in this optical depth range characteristically have $W/R \sim 0.5$ (because optical depth rises more slowly with decreasing impact parameter) and possess narrow, very dark cores. Surface brightness increases in a nearly linear fashion from core to rim in this class of model, and the ratio of rim to core brightness is shown to be a useful probe of the maximum cloud opacity.

Red- and blue-light surface brightness measurements made along the major and minor axes of the globule and smoothed to a scale of 21″ are shown in Figure 2. These results demonstrate that the cloud is centrally condensed. The ratio of rim width to cloud radius, averaged with respect to axis and color, is $\langle W/R \rangle = 0.6$ if half-power dimensions are used; if one instead defines the outer cloud radius as that point at which the surface brightness reaches that of the adjacent sky, a value $\langle W/R \rangle = 0.45$ is obtained. Both values are much closer to that characterizing the r^{-2} model of WS than they are to the uniform-density case. Indeed, the excellent agreement in shape between the curves of Figure 2 and those presented by WS suggests that the actual density distribution in the globule may not be too different from r^{-2} (see § IV*e*).

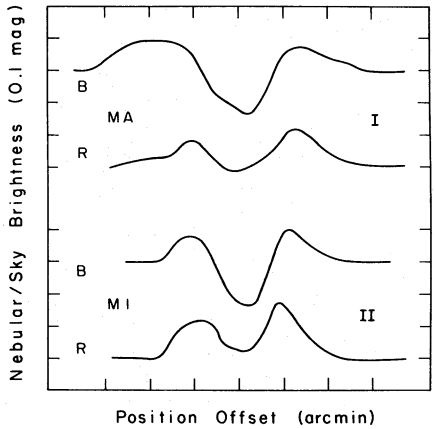

FIG. 2.—Surface brightness of the globule vs. position along the major and minor axes (I and II on Fig. 1), in both red (R) and blue (B) colors. The tracings were made from enlargements of the POSS O and E prints of the globule region using a microdensitometer and have been smoothed to 21″ resolution.

The rim-to-core brightness ratios measured from Figure 2 also allow one to roughly ascertain the maximum visual extinction through the globule center. (A more exact treatment is possible if photometrically calibrated plates are available, as discussed by FSW.) Assuming a grain albedo of 0.5 and scattering phase function asymmetry parameter $g = 0.7$ (FSW), the rim-core brightness ratio leads to the estimate $A_v(\max) \approx$ 3–5 mag, after correcting the brightness ratio for the contribution of the DGL using the values of FSW or Roach (1967).

c) Radio

Radio observations are summarized in Table 1. Listed for each map position are molecular species and transition, peak line radiation temperatures, T_R, (cf. Kutner and Ulich 1981) determined as described below, line velocity centroid with respect to the local standard of rest, and line full width at half-intensity, Δv. Because data taken with the autocorrelation spectrometer are Hamming filtered prior to taking the Fourier transform, the $J = 1 \rightarrow 0$ spectra are instrumentally broadened. This effect is most pronounced for narrow lines and, for our $C^{18}O$ spectra, typically amounts to a 10% width enhancement. All $J = 1 \rightarrow 0$ line widths reported in the table have been corrected for this instrumental broadening, assuming intrinsically Gaussian line shapes.

Line radiation temperatures were obtained from the chopper-wheel–calibrated antenna temperatures by calculating the forward coupling efficiency of the FCRAO and MWO antennas for a uniform disk 3′ in diameter. To do so, measured antenna response patterns at the appropriate frequencies were utilized. The coupling efficiencies obtained for the FCRAO data were found to be close to the main beam efficiencies so that results are relatively insensitive to the assumed source size. Calibration of the $J = 2 \rightarrow 1$ data is somewhat more uncertain because the globule was not mapped at 1 mm and because the MWO antenna pattern contains three fairly high level sidelobes, displaces some 2′–3′ from the main beam axis. We estimate the final radiation temperature calibrations to be accurate to about 15% and 20% for the $J = 1 \rightarrow 0$ and $J = 2 \rightarrow 1$ data, respectively.

A panel of representative spectra toward the center of the globule is shown in Figure 3. If, as is usual, the CO $J = 1 \rightarrow 0$ line is assumed to be thermalized and optically thick, the peak observed radiation temperature implies a characteristic excitation temperature $T_x \approx 14$ K for the region in which the line is formed. As a first approximation this may be adopted as the kinetic

TABLE 1A

$J = 1 \rightarrow 0$ CO AND ^{13}CO MAPPING RESULTS

Offset $\Delta\alpha, \Delta\delta$ (arcmin)	^{12}CO				^{13}CO			
	T_R[a]	(ΔT)[b]	Δv[c]	$\langle v \rangle$[d]	T_R[a]	(ΔT)[b]	Δv[c]	$\langle v \rangle$[d]
3, 1	2.1	(0.7)	[e]	[e]	...	...	...	...
2, 2	3.9	(0.7)	0.50	−11.23	...	...	...	...
2, 1	4.3	(1.1)	0.51	−11.28	2.5	(0.4)	≤0.53	−11.22
2, 0	2.9	(1.3)	[e]	[e]	...	...	...	...
1.7, 0	3.7	(0.4)	0.55	−11.30	...	...	...	...
1, 3	4.0	(0.6)	0.32	−11.19	...	...	...	...
1, 2	4.9	(1.1)	0.45	−11.34	2.1	(0.4)	0.32	−11.23
1, 1	8.1	(0.6)	0.58	−11.35	4.4	(0.5)	0.36	−11.29
1, 0	7.4	(0.9)	0.42	−11.33	1.8	(0.3)	0.35	−11.29
1, −1	3.1	(0.5)	0.55	−11.3	...	...	...	...
0, 3.4	2.5	(0.7)	0.26	−11.26	...	...	...	...
0, 3	0.8	(0.6)	[e]	[e]	0.3	(0.4)	[e]	[e]
0, 2	7.5	(1.2)	0.58	−11.35	3.6	(0.4)	0.34	−11.29
0, 1.7	9.1	(0.6)	0.29	−11.30	...	...	...	...
0, 1	10.7	(1.0)	0.53	−11.33	5.9	(0.4)	0.38	−11.30
0, 0	10.4	(0.3)	0.47	−11.32	4.6	(0.2)	0.35	−11.28
0, −1	5.1	(1.1)	0.42	−11.36	1.1	(0.4)	[e]	[e]
0, −1.7	3.8	(0.4)	0.52	−11.33	...	...	...	...
−1, 2	2.3	(1.0)	[e]	[e]	0.6	(0.6)	[e]	[e]
−1, 1	9.2	(0.9)	0.45	−11.30	2.4	(0.3)	0.43	−11.23
−1, 0	10.4	(1.0)	0.44	−11.32	3.0	(0.5)	0.32	−11.23
−1, −1	7.2	(0.4)	0.42	−11.25	0.7	(0.4)	[e]	[e]
−1, −2	1.5	(0.5)	0.32	−11.25	...	...	...	...
−1.7, 0	4.1	(0.6)	0.36	−11.21	...	...	...	...
−2, 2	2.5	(0.6)	[e]	[e]	...	...	...	...
−2, 1	1.0	(1.0)	[e]	[e]	...	...	...	...
−2, 0	5.0	(0.9)	0.64	−11.36	0.5	(0.5)	[e]	[e]
−2, −1	2.3	(0.5)	0.24	−11.26	...	...	...	...

TABLE 1B

OTHER SPECTRAL-LINE RESULTS

Offset $\Delta\alpha, \Delta\delta$ (arcmin)	Molecule	J'–J	T_R[a]	(ΔT)[b]	Δv[c]	$\langle v \rangle$[d]
0, 2.75	^{13}CO	2–1	0.6	(0.2)	[e]	[e]
0, 2	C^{18}O	1–0	0.2	(0.2)	[e]	[e]
0, 1.75	^{12}CO	2–1	5.8	(0.7)	0.48	−11.44
	^{13}CO	2–1	3.0	(0.2)	0.36	−11.41
0, 1	C^{18}O	1–0	1.3	(0.16)	0.23	−11.37
0, 0.75	^{12}CO	2–1	6.9	(0.3)	0.57	−11.40
	^{13}CO	2–1	3.4	(0.2)	0.40	−11.33
	C^{18}O	2–1	0.7	(0.2)	[e]	−11.34
0, 0	C^{18}O	1–0	1.4	(0.12)	0.19	−11.31
0, −0.25	^{12}CO	2–1	7.0	(0.4)	0.55	−11.40
	^{13}CO	2–1	2.6	(0.2)	0.37	−11.39

[a] Radiation temperature of line peak, K (§ IIIc).
[b] RMS noise of spectrum.
[c] Line full width at half-intensity, km s^{-1}.
[d] Line centroid velocity, km s^{-1}.
[e] Spectrum too noisy for reliable determination.

temperature of the cloud, subject to the following qualifications. (1) As is clear from Table 1, significant gradients in T_x can be inferred to exist over the cloud, since ^{13}CO is observed at locations where the CO radiation temperature has fallen well below its peak value. (2) Depending upon the nature of the internal velocity field, the inferred 14 K excitation temperature may not pertain to the central regions of the cloud—the cloud core may be colder than 14 K. Ultimately, both points (1) and (2) demand that any inferred thermal structure of the cloud be checked against the observations using a line formation model, as described in § IV.

The spectral lines depicted in Figure 3 are unusually narrow, ranging from $\Delta v = 0.60$ km s^{-1} for the CO $J = 2 \rightarrow 1$ line to $\Delta v = 0.23$ km s^{-1} for the C^{18}O $J = 1 \rightarrow 0$ line. No statistically significant positional varia-

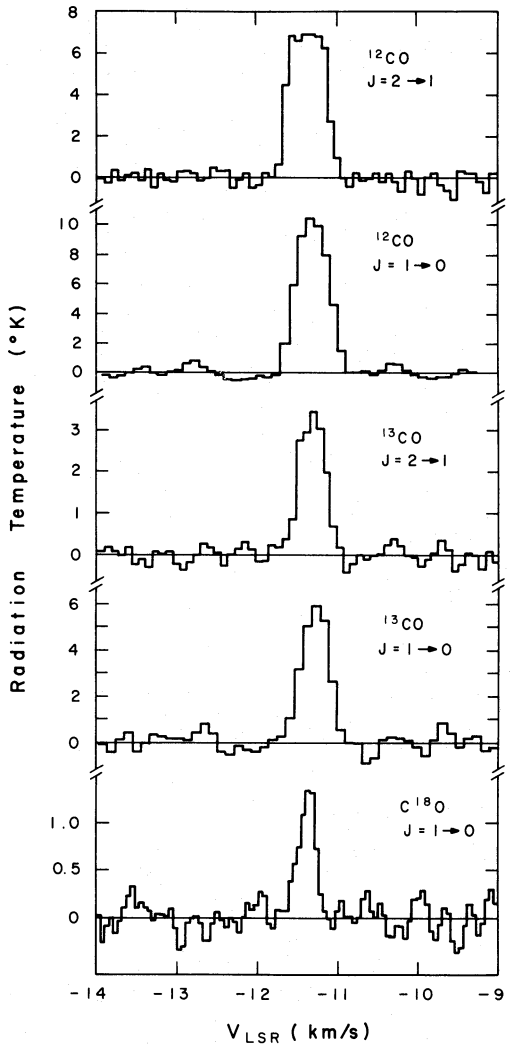

FIG. 3.—Carbon monoxide spectra toward position (0, 1); this is the location of peak CO and ^{13}CO $J = 1 \rightarrow 0$ line intensity in the cloud. Note the extremely narrow C^{18}O line.

tions in the v_{LSR} of any mapped species are evident in the data. This implies that any systematic velocity shift across the cloud due to shear or rotation has a total amplitude ≤ 0.07 km s^{-1}. Likewise, the absence of statistically significant positional fluctuations in v_{LSR}—which would add in quadrature with the observed line dispersions to yield the total rms flow amplitude for the cloud—indicates that the globule possesses a singularly low internal velocity dispersion compared with those of most other interstellar dark clouds. The nature of the velocity field is discussed in detail in § IV*a*.

Table 2 lists values of ^{13}CO LTE column density, calculated in the manner described by Dickman (1978*b*), at each location in the globule where concurrent CO and ^{13}CO observations were made. Also listed for each position are equivalent visual extinctions, obtained from the relations developed in Appendix B. The excellent agreement between the peak visual extinction derived

TABLE 2

^{13}CO COLUMN DENSITIES AND INFERRED VISUAL EXTINCTIONS

Offset[a] ($\Delta\alpha$, $\Delta\delta$)	N_{13}(LTE) (10^{15} cm^{-2})	A_v[b] (mag)
(2, 1)	0.76	0.8
(1, 2)	0.73	0.7
(1, 1)	2.10	1.3
(1, 0)	0.65	0.7
(0, 3)	<0.10	<0.3
(0, 2)	1.50	1.1
(0, 1)	3.30	1.7
(0, 0)	2.13	1.3
(0, −1)	0.37	0.5
(−1, 2)	<0.18	<0.4
(−1, 1)	1.15	0.9
(−1, 0)	1.14	0.9
(−1, −1)	<0.23	<0.4
(−2, 0)	<0.15	<0.3
Unsampled[c]	≤2	≤2.2

[a] Offset in arcmin from $\alpha(1950) = 0^h36^m17^s.0$, $\delta(1950) = 52°34'37''$.

[b] Equivalent visual extinction from N_{13}(LTE). See Appendix B.

[c] Based upon ^{13}CO data, weak but detectable emission may be expected at (1, 3), (1, −1), and (2, 0). Based upon ^{13}CO intensities elsewhere in cloud, a total column density $\leq 2 \times 10^{15}$ may be expected from all three locations. Value for A_v assumes equal contributions.

in this fashion, 1.7 mag, and the average core extinction deduced from the star counts (§ III*b*), 1.85 mag, should be noted. Assuming a standard gas-to-extinction ratio for the globule ($N_{H_2}/A_v \approx 10^{21}$ cm^{-2} mag^{-1} [Bohlin, Savage, and Drake 1978]) and including a $\sim 10\%$ correction by number for helium (Allen 1973) then leads to the following mass for the portion of the cloud producing measurable ^{13}CO emission:

$$M_{13} = 0.6(d/600 \text{ pc})^2 \sum_i A_v(i)\, M_\odot , \qquad (2)$$

where d is the distance to the globule, and $A_v(i)$ is the extinction in each 1′ square listed in Table 2. Taking $d = 600$ pc (Appendix A) and using the tabulated A_v gives $M_{13} = 7.3\ M_\odot$.

The total cloud mass must, of course, exceed M_{13}. Both the mean CO and photometric radii, defined, respectively, by the outer edge of the ^{12}C^{16}O emission and the point at which the (blue) surface brightness of the cloud is comparable to that of the sky, have values $\sim 3'$ and $\sim 2'.5$, somewhat larger than the $\sim 2'$ mean ^{13}CO radius. If the CO radius is assumed to define the true cloud size, for example, and a characteristic volume density $n_{H_2} \sim 150$ cm^{-3} is assigned to the outer annulus not probed by ^{13}CO, the total cloud mass is then of order 10 $M_\odot$. We shall consider this issue again in § IV*e*.

IV. CLOUD MODELS

Some basic properties of the globule deduced from the observations are summarized in Table 3. In this section

TABLE 3

OBSERVATIONALLY INFERRED PARAMETERS
$\Delta \equiv$ (Globule Distance/600 pc)

Quantity	Comments/Source	Measured	Inferred
Ellipticity	[a]	1.3	1.3
Mean radius, opaque core	POSS O print	0.7	0.12Δ pc
Mean radius, ^{13}CO region	$J = 1 \rightarrow 0$ data	2′	0.35Δ pc
Mean radius, CO region	$J = 1 \rightarrow 0$ data	3′	0.52Δ pc
Mean radius, photometry	to sky brightness	2.5	0.43Δ pc
Characteristic kinetic temperature	CO intensity	14 K	14 K
Mass interior to R_{13}	^{13}CO data[b]	...	$\geq 7.3\Delta^2\ M_\odot$
Mean core extinction	POSS E star counts	1.9	1.9 mag
Mean core extinction	^{13}CO column density[b]	1.7	≥1.7 mag
Maximum cloud extinction	photometry	3–5	3–5 mag

[a] (Major diameter)/(minor diameter). Measured with respect to photometric outer half-power levels.
[b] See § IIIc and Appendix B.

models of the globule are considered with the goal of accounting for these attributes. In addition, multilevel non-LTE CO line formation calculations consistent with the final model adopted are presented, in order to gauge the adequacy with which they represent the spectral-line data.

A common starting point in the determination of a cloud's dynamical state is to consider the two most extreme characterizations of the internal velocity field—systematic and fully disordered flows—and to examine each on the basis of its relative merits. As remarked earlier, it is usually impossible to specify turbulent model states for dark clouds with precision because such configurations are observationally constrained to be supersonic. We begin by demonstrating that in the present case this is not so.

a) *Turbulence*

An upper limit to the amplitude of turbulent motions within the globule can be obtained by assuming the cloud to be stable. In that case, all the gas motions which broaden the CO lines must be spatially disordered. For simplicity, it will be assumed that the velocity field is homogeneous and isotropic, and described by an amplitude $\langle v^2 \rangle^{1/2} \equiv \sigma_0$ on scales larger than the flow correlation length.

To extract σ_0 from the observations it should be recalled that if the correlation length is sufficiently small (an issue discussed in more detail in § IV*f*), optically thick spectral lines will be substantially broadened by saturation effects (Traving 1975; Dickman and Kleiner 1983). To minimize this potential effect, σ_0 should be estimated from the least saturated available transition, which in the present case is the $C^{18}O$ $J = 1 \rightarrow 0$ line.

Assuming a Gaussian distribution function for the random motions, an optically thin spectral line observed with an antenna beam whose projected size on the cloud is larger than the flow correlation length will be Gaussian in shape (Dickman and Kleiner 1983). The latter criterion is not a very stringent one for the 47″ FCRAO beam at 109.8 GHz (since at 600 pc the HPBW subtends ~0.2 pc, about one-fifth the cloud diameter), so that in this case the full width at half-intensity of an optically thin line is related to the e^{-1} dispersion of the profile by $\Delta v = 2(\ln 2)^{1/2}\sigma$. The dispersion σ is the root mean squared sum of thermal and turbulent velocity fluctuations along the line of sight:

$$\sigma^2 = 2\left(\frac{kT}{m_{\rm CO}} + \sigma_l^2\right), \tag{3}$$

where T is the kinetic temperature, taken as uniform, $m_{\rm CO}$ is the CO molecular mass, and σ_l^2 is the variance of the line-of-sight velocity field fluctuations. For an isotropic flow, σ_l^2 is related to the three-dimensional rms fluctuation amplitude via

$$\sigma_l^2 = \tfrac{1}{3}\sigma_0^2 .$$

Combining these relations gives

$$\sigma_0 = \left[3\left(\frac{\Delta v^2}{8 \ln 2} - \frac{kT}{m_{\rm CO}}\right)\right]^{1/2} . \tag{4}$$

Taking $T = 14$ K (Table 3) and $\Delta v = 0.23$ km s^{-1} for the $C^{18}O$ line (Table 1) leads to

$$\sigma_0 = 0.12 \text{ km s}^{-1} \tag{5}$$

for the *maximum* turbulent velocity dispersion; the nature of relation (5) as an upper limit arises not only because we have *assumed* the cloud to be stable (so that Δv_{18} is uncontaminated by collapse or expansion) but also because some slight saturation of the $C^{18}O$ line at the (0, 1) position cannot be excluded.

The dispersion given by relation (5) is remarkable in several respects. Denoting the mean particle mass in the cloud by μ, the adiabatic sound speed for the cloud is $c_a = (5kT/3\mu)^{1/2} \approx 0.28$ km s^{-1}, so that the adiabatic Mach number $M_a \leq 0.4$; any turbulence in the cloud is thus subsonic by a wide margin. While localized, nearly sonic condensations within certain molecular clouds, notably those in Taurus (Myers and Benson 1982), have been previously studied, to our knowledge the globule is the first isolated unit cloud to be revealed as fully subsonic. As a result, vigorous

shock wave dissipation, which should plague a supersonic turbulent flow, will be absent here, greatly prolonging the lifetime of the turbulence. Indeed, if the turbulence is treated as a field of sound waves of random phase, one can show that motions of amplitude 0.1 km s^{-1} can be maintained against viscous decay and boundary leakage by coupling to the $\sim 3 \times 10^{-25}$ ergs s^{-1} cm^{-3} power density driven by supernovae (Cox 1979) in the intercloud medium (see also Spitzer 1982).

Turbulence produces a supportive stress in addition to thermal pressure. On scales larger than the correlation length, this dynamical pressure is $\rho\sigma_0^2/3$, so that the ratio of thermal to turbulent pressure is $9/5M_a^2$. In the present case this ratio is approximately 10. Therefore, any equilibrium state in which magnetic fields may be ignored will be thermally, not dynamically, dominated. The turbulent stress can be characterized as an additional effective temperature $T_{\rm eff} = \mu\sigma_0^2/3k$, roughly 1.5 K in the present case. The total equivalent temperature of the cloud is then $\sim$15.5 K if the 14 K fiducial temperature of Table 3 is used.

b) *Saturation Broadening and Implications for Systematic Motions*

The CO and ^{13}CO lines in the globule are considerably wider than their C^{18}O counterparts. To the extent that a uniformly excited microturbulent line formation scheme can be taken to approximate the cloud, the line widths of the more abundant isotopic species appear to be consistent with saturation broadening of the underlying velocity dispersion exhibited by the C^{18}O line. Assuming a Gaussian line profile function, a spectral line with core opacity τ_0 in such a model will display an enhanced width Δv compared with a thin line having width Δv_0:

$$\left(\frac{\Delta v}{\Delta v_0}\right) = (\ln 2)^{-1/2} \times \left[-\ln\left\{\tau_0^{-1} \ln\left[\frac{2}{\exp(\tau_0)+1}\right] + 1\right\}\right]^{1/2} . \quad (6)$$

Comparing the observed CO and ^{13}CO line widths at the (0, 1) position of the globule using $\Delta v_{18} = 0.23$ km $s^{-1} = \Delta v_0$, and solving equation (6) for τ_0 gives $\tau_{12}(2\text{–}1) \sim 50$, $\tau_{12}(1\text{–}0) \sim 30$, $\tau_{13}(2\text{–}1) \sim 6$, and $\tau_{13}(1\text{–}0) \sim 4$. Considering the crudeness of the line formation model used here, these are entirely reasonable values, and they suggest that the ^{13}CO transitions observed are probably subthermally excited in the globule, a common condition in dark nebulae (e.g., Dickman, McCutcheon, and Shuter 1979).

While suggestive, the above demonstration does not, of course, prove that systematic motions are absent in the globule. Even granting the existence of turbulent motions of amplitude 0.1 km s^{-1}, we have accounted for neither the inhomogeneous character of the cloud nor, more importantly, the possibility of a moderate turbulent flow scale which would inhibit the degree of saturation broadening (Traving 1975). We can therefore merely note that from a line formation standpoint, an ordered flow is not *a priori* required to replicate the line widths observed for the optically thick species toward the center of the globule. Further support for an essentially static cloud configuration does, however, follow from an assessment of the globule's equilibrium, carried out below.

c) *Global Equilibrium*

If dissipative forces due to turbulence are neglected—a reasonable assumption in view of the foregoing constraints regarding the flow amplitude—the cloud will obey the virial theorem (e.g., Spitzer 1978). Treating the cloud as spherical and ignoring magnetic fields for the moment, a stable configuration must obey the following energy relation:

$$4\pi R^3 p_0 + \frac{GM^2}{R} = 3M\left(\frac{kT}{\mu}\right) + M\sigma_0^2 + \frac{1}{9}Mv_0^2 . \quad (7)$$

Here M, R, and T are the cloud's mass, radius, and temperature, respectively, σ_0 is the three-dimensional turbulent velocity dispersion, p_0 is the external pressure of the intercloud medium, and v_0 is the equatorial rotational velocity of the cloud, discussed below. The other symbols have their usual meaning. The centrally condensed state of the cloud has been accounted for approximately by employing a coefficient of unity in the gravitational term rather than the three-fifths appropriate to a uniform mass distribution; this replacement is exact if the density profile within the cloud goes as r^{-2}, and the mass of the cloud is finite.

To estimate the terms in equation (7) numerically, we adopt Myers' (1978) value of $p_0 = 3700k$ dyn cm^{-2}, utilize a CO radius of 0.5 pc, and characteristic cloud kinetic temperature of 14 K (Table 3), as well as the turbulent velocity dispersion given by relation (5). To characterize the total cloud mass interior to $R = 0.5$ pc, the total mass estimate $M = 10\ M_\odot$ (§ IIIc) may be used. In units of 10^{43} ergs, the external pressure, gravitational, thermal, and turbulent energies are found to be 2.4, 1.7, 3.0, and 0.3. Ignoring the rotational energy term, the ratio of compressive to support energies is about 1.2. This is close to the value of unity for a perfectly stable cloud, perhaps surprisingly so, given the uncertainty in the various parameters entering equation (7). The fact that external pressure plays a comparable if not slightly dominant role compared with self-gravity in confining the globule is a not entirely unexpected consequence of the cloud's small mass and rather diffuse state.

Rotation has been ignored above on observational grounds. The rotational energy in equation (7) was derived assuming solid-body rotation weighted by the same r^{-2} density distribution used in computing the gravitational energy. The ratio, Υ, of rotational to gravitational energy is

$$\Upsilon \equiv (Rv_0^2/9GM) . \quad (8)$$

For rotation to be significant (of importance comparable,

say, to turbulence), one requires $\Upsilon \geq 0.1$. But the observational data (§ IIIc) constrain the value $2v_0 \sin(i) \leq 0.07$ km s^{-1}, where i is the inclination angle of the rotation axis with respect to the line of sight. In order to satisfy equation (8) with $\Upsilon \geq 0.1$ then requires $|i| \leq 7°$. This value is so small as to make it statistically unlikely that rotation plays much of a role in ordering the cloud. Moreover, if rotation at the stipulated axis tilt is in fact present, it can hardly be responsible for the observed ellipticity of the globule, since the cloud would then be flattened essentially along, not normal to, the line of sight.

d) Magnetic Fields

The near-equality of the compressional and supportive energies found above is somewhat surprising from the standpoint of any magnetic field within the globule. To make up the computed deficit, δ, between the two classes of energies requires only a mean-square field strength for the cloud (Spitzer 1978) of $\langle B^2 \rangle \approx 3\delta/R^3 \approx (2.5\ \mu\text{G})^2$. The associated field energy would then be about 25% of the turbulent and thermal energies when averaged over the cloud, that is, of only marginal importance to the energy budget but potentially still crucial in fixing the local structure of the globule.

However, 2.5 μG is close to the mean 2–3 μG strength of the fossil field usually assumed to pervade the interstellar medium. This might suggest that the globule formed in a region of abnormally low magnetic field strength, provided its formation was gentle enough to permit field amplification by (anisotropic) flux freezing (Mouschovias 1976). But a violent formation event is almost surely required to explain the present state of the cloud, since at typical H I cloud densities and temperatures the spontaneous occurrence of a 10 $M_\odot$ condensation would be most unlikely. The fate of an embedded 2 μG field under such circumstances is at best ambiguous. Without any observational constraints on the present internal field of the cloud, the role of magnetic forces in shaping the globule must, in our view, be regarded as entirely speculative.

It therefore appears prudent to treat the cloud without the introduction of an additional (and observationally free) parameter in the guise of the magnetic field strength and to examine the ensuing nonmagnetic models on their own merits. The one potential difficulty with this strategy is that a natural origin for the observed ellipticity of the cloud is sacrificed (cf. Mouschovias 1976). However, an ordered internal magnetic field is not the sole mechanism capable of elongating the cloud. External pressure anisotropy (Dyson 1973) is an attractive alternative which would be a natural consequence of relative motion of the globule with respect to its surroundings. The windblown appearance of many isolated dark nebulae, evinced by the presence of one sharp and one diffuse edge (cf. E. E. Barnard as quoted by Lynds 1968), suggests an external, gas dynamic origin. This morphology is shared by the present globule, as indicated by the brightness tracings of Figure 2. The geometric mean of the outer half-power points along the major axis does not coincide with the brightness minimum (i.e., core) of the cloud; the latter is displaced by about 25% of the axis diameter from the geometric center of the globule.

e) Detailed Hydrostatic Cloud Models

The construction of detailed hydrostatic models of the globule is desirable for several reasons. First, by imposing *a priori* the requirement of equilibrium, one can see in a conveniently parametric fashion whether global attributes of the model clouds, such as mass, radius, visual extinction, etc., can be successfully matched to their observationally determined counterparts. This amounts to a parametric exploration of the virial stability criterion (7) which implicitly accounts exactly for model-dependent variations in the energy coefficients, as well as for factors such as kinetic temperature gradients (thus far ignored). Second, the models offer a means to characterize the radial variation of local parameters such as density and kinetic temperature, which are required for line formation modeling. Third, they provide additional physical insight into possible consequences of the equilibrium states.

For simplicity, we shall retain our previous assumption of spherical symmetry in what follows. It is difficult to see how this could lead to very serious errors provided the physics of our models is complete, since the observational data are in any case rather coarse in spatial resolution.

Neglecting both rotation and magnetic fields, the models must satisfy the usual hydrostatic balance equation for a sphere, subject to the boundary conditions that (i) the edge pressure is continuous and equal to the intercloud pressure, p_0, and (ii) the central density $\rho(0)$ is nonsingular. The cloud is treated as an ideal gas, so that the local pressure $p(r) = n(r)kT(r)$, where $n(r)$ is the number density of the gas at r, and $T(r)$ is the effective temperature, which includes both thermal $T_K(r)$ and turbulent components:

$$T(r) = T_K(r) + \mu\sigma_0^2/3k\ . \tag{9}$$

Equation (9) embodies implicitly the assumption that the turbulence is isotropic, homogeneous, and possesses a correlation length smaller than the scale of any thermal or density gradients.

In order to specify the models completely, an equation of state is required. We shall consider two of these. The first is the simplest approximation to the observational data, viz., an isothermal cloud with $T(r) = 16$ K. The second attempts to refine this picture by accounting for the edge heating produced both by a decreased CO coolant abundance, as well as by incident peripheral UV; both effects are apt to be significant because the globule is of low visual opacity. A rigorous treatment of this case would require use of a full chemical cooling network, as well as one desired result of the hydrostatic models themselves, that is, the density distribution in the globule envelope. To avoid a massive coupled calculation of this type, we instead adopt an

equation of state based upon recent work by de Jong, Dalgarno, and Boland (1980), who studied the chemical, thermal, and dynamical equilibrium of one-dimensional molecular cloud configurations. Over a wide range of model parameters they find that the thermal pressure of a gas parcel subject to a constant visual extinction goes as $p \sim \rho^{2/3}$. Although positional extinction variations must cause local deviations from this simple scaling relation in an actual cloud, examination of the pressure-density law obtained by de Jong *et al.* for a uniformly turbulent cloud suggests that within the uncertainties inherent in their calculations, an equation of state of the form

$$p(r) = K\rho^{2/3}(r) \tag{10}$$

may be adopted. In what follows, the parameter $K \equiv [kT(0)/\mu]\rho(0)^{1/3}$ will be assumed to vary for each equilibrium configuration only through variations in central density; that is, the central temperature of the models will be assumed constant.

Both classes of model are therefore described by a state equation of the form

$$p(r) = K[\rho(r)]^{1+1/N}, \tag{11}$$

where $N = \infty$, -3 for the isothermal and hot-edged cases, respectively. This relation defines a polytrope of index N, and specification of the hydrostatic model states is thus reduced to determining two sets of pressure-bounded polytropic model solutions, one for each index (e.g., Chandrasekhar 1939; Shu *et al.* 1972).

To construct solution sequences, one chooses the bounding pressure, $p(R) \equiv p_0$, and central effective temperature, T_0. By introducing a dimensionless length $\xi \equiv r/\alpha(\xi_1)$ which maps the interval $r = [0, R]$ into $\xi = [0, \xi_1]$, so that $\xi_1 = R/\alpha(\xi_1)$, the hydrostatic balance equation is transformed into standard Lane-Emden form (e.g., Milne 1930; Chandrasekhar 1939). The constant $\alpha(\xi_1)$ depends upon the polytropic index, N, as well as upon p_0 and T_0. Any particular solution with a given index is specified uniquely by the value ξ_1; one can think of ξ_1 as fixing the central density of the solution, since $n(0)$ is a single-valued function of ξ_1.

As shown in Table 4, once ξ_1 is specified, the mass and radius of an equilibrium model are then fixed in terms of a standard Emden function of index N. Tabular solutions of the Emden functions for $N = \infty$ and -3.0 are given by Milne (1930) and Viala and Horedt (1974), respectively. The radial variations of density and effective temperature within the model cloud are also easily established with these functions (Table 4). Peak visual extinction and the variation of extinction with projected offset from the model cloud center can be obtained by numerically integrating the density profile along the appropriate sight line, assuming a fixed gas-to-extinction ratio, $A_v = 10^{-21}N_{H_2}$. A comparison can then be made between the observationally determined parameters of Table 3 and their model counterparts. In effect, the goal is to determine for a given index whether a value of ξ_1 exists which produces reasonable agreement between the two parameter sets.

A solution sequence depends upon the initial choice of boundary pressure and central temperature (Table 4). Scaling of the most important global model attributes with respect to these quantities for fixed ξ_1 is given by

$$\begin{aligned} M &\sim p_0^{-1/2}, \quad T_0^2; \\ R &\sim p_0^{-1/2}, \quad T_0; \\ A_v &\sim p_0^{1/2}. \end{aligned} \tag{12}$$

TABLE 4

PRESSURE-BOUNDED POLYTROPES

Quantity	Isothermal	Hot-edged
Boundary pressure	$p(R)$	$p(R)$
Central temperature	T_0	T_0
Central isothermal soundspeed	$C_i = (kT_0/\mu)^{1/2}$,	$C_i = (kT_0/\mu)^{1/2}$
Length scale	$R_* = C_i^2[2\pi G p(R)]^{-1/2}$	$R_* = C_i^2[2\pi G p(R)]^{-1/2}$
Density scale	$n_* = p(R)/kT_0$	$n_* = p(R)/kT_0$
Mass scale	$M_* = R_* C_i^2/G$	$M_* = R_* C_i^2/G$
Polytropic index, N	∞	-3.0
Emden equation[a]	$\nabla^2 u(\xi) = \exp[-u(\xi)]$	$\nabla^2\theta(\xi) = \theta^{-3}(\xi)$
Dimensionless radial variable	$\xi = \{2\exp[u(\xi_1)]\}^{1/2}(r/R_*)$	$\xi = \theta(\xi_1)(r/R_*)$
Core density	$n_0 = n_* \exp[u(\xi_1)]$	$n_0 = n_*\theta^2(\xi_1)$
Cloud radius	$R = R_*[\xi\exp(-u)/2]_{\xi_1}$	$R = R_*[\xi\theta^{-1}(\xi)]_{\xi_1}$
Cloud mass[b]	$M = M_*\{[\exp(-u)/2]^{1/2}\xi^2 u'(\xi)\}_{\xi_1}$	$M = 2M_*[\xi^2\theta'(\xi)/\theta(\xi)]_{\xi_1}$
Edge density	$n(R) = n_*$	$n(R) = n_*\theta^{-1}(\xi_1)$
Edge temperature	$T(R) = T_0$	$T(R) = T_0\theta(\xi_1)$
Density profile	$n(\xi) = n_0\exp[-u(\xi)]$	$n(\xi) = n_0\theta^{-3}(\xi)$
Temperature profile	$T(\xi) = T_0$	$T(\xi) = T_0\theta(\xi)$

[a] $\nabla^2 = \xi^{-2}d_\xi(\xi^2 d_\xi)$. Tabulations of the Emden functions are given by Milne 1930 for $N = \infty$, and by Viala and Horedt 1974 for $N = -3.0$.

[b] The notation $f'(\xi) \equiv d_\xi f(\xi)$ is used.

The dependence of other quantities of interest upon p_0 and T_0 may be worked out easily from Table 4.

Model sequences with $N = \infty$ and -3.0 both lead naturally to centrally condensed configurations. This is depicted in Figure 4, where normalized density has been plotted for each index as a function of the dimensionless scale ξ. At large distances from the model origin, neglecting a small, oscillatory ξ-dependent term, densities go as ξ^{-2} and $\xi^{-1.5}$ for the isothermal and hot-edged models, respectively (Chandrasekhar 1939; Viala and Horedt 1974). Either result is consistent with our previous estimate for the density law in the globule envelope based upon the photometric data (§ III*b*[ii]). Both types of model are stable with respect to convection and to small radial perturbations. However, the isothermal models possess a critical linear scale, ξ_c, beyond which equilibrium solutions are unstable with respect to an increase in external pressure (Bonnor 1956; Spitzer 1968). If an equilibrium configuration with $\xi_1 > \xi_c$, initially bounded by p_0, is subjected to an isotropic pressure excess, δp_0, no stable isothermal configuration of the same mass can exist in equilibrium with the new pressure $p_0 + \delta p_0$; the model cloud must collapse.

The solution sequence with $N = -3$ lacks this instability. This may appear surprising at first, particularly since instabilities of this type are implicit in the structure of a wide range of self-gravitating, pressure-bounded polytropic systems (Bonnor 1958; Kimura 1981) and have been discussed specifically for the $N = -3$ case (Shu *et al.* 1972). However, it is readily demonstrated that the pressure instability in a sequence of polytropic configurations of constant mass is closely tied to the requirement that the solution set be characterized by a *single* value of the proportionality factor K in equation (10). Owing to the assumption of constant core temperature made above, this is not the case for the sequence of warm-edged hydrostatic models which we generate; rather, each equilibrium configuration possesses its own proportionality constant, K. The usual Bonnor stability criterion may in fact be applied to any hydrostatic solution of constant mass and core temperature described by Table 4, and it is easily shown that the configuration is stable with respect to external pressure increases.

The isothermal model sequence which results from choosing $p_0/k = 3700$ K cm^{-3} and $T_0 = 16$ K is shown in Figure 5*a*. Mass, radius, central H_2 number density, and visual extinction through the model center have been plotted as functions of ξ_1. The critical scale ξ_c, which is about 6.4 for isothermal polytropes (Spitzer 1968), is also shown. In Figure 5*b*, the analogous solution sequence for the hot-edged models has been plotted with the addition of the edge temperature. It should be noted that for the $N = -3.0$ sequence a core temperature of only 8 K was chosen, about the lowest value consistent with cosmic-ray heating of the cloud (Goldsmith and Langer 1978). This choice stems from the fact that because the cloud heats up with radius, optically thick CO emission cannot be expected to accurately reflect the central temperature of the cloud. That such a thermal structure is in fact capable of reproducing the observed CO intensities toward the inner regions of the globule is demonstrated in the next section.

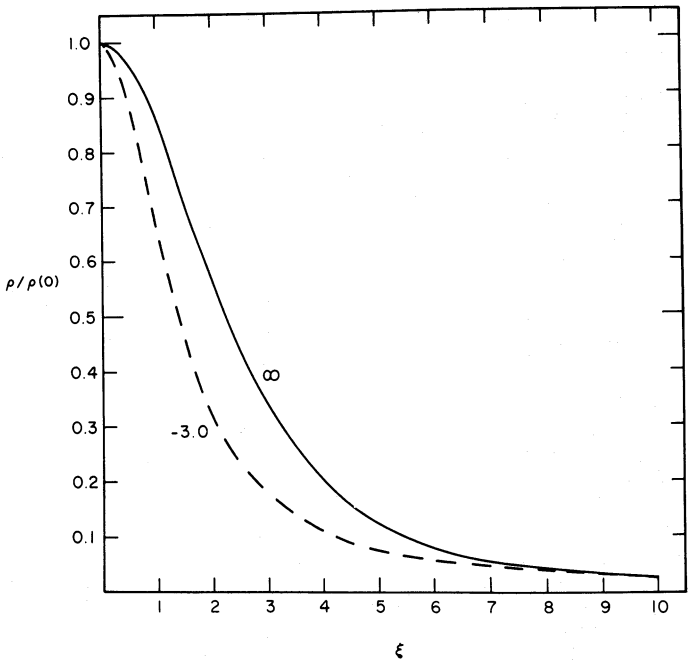

FIG. 4.—Normalized density profiles for the isothermal ($N = \infty$) and hot-edged ($N = -3$) hydrostatic models (cf. § IV). The abscissa, ξ, is proportional to radial distance from the model center. Its maximum allowable value, ξ_1, depends only upon the central density of the model, once the core temperature and boundary pressure of the model have been fixed (§ IV*e*).

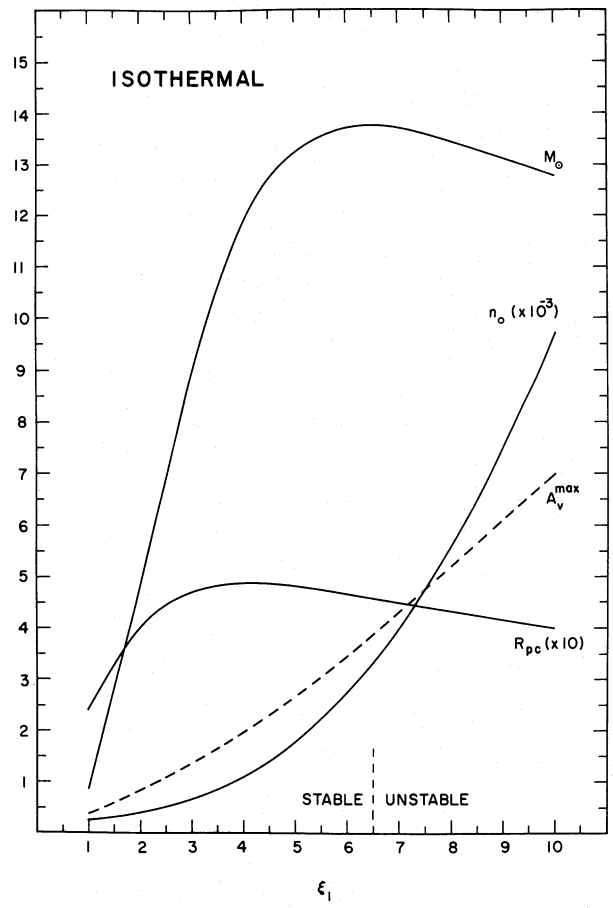

FIG. 5a

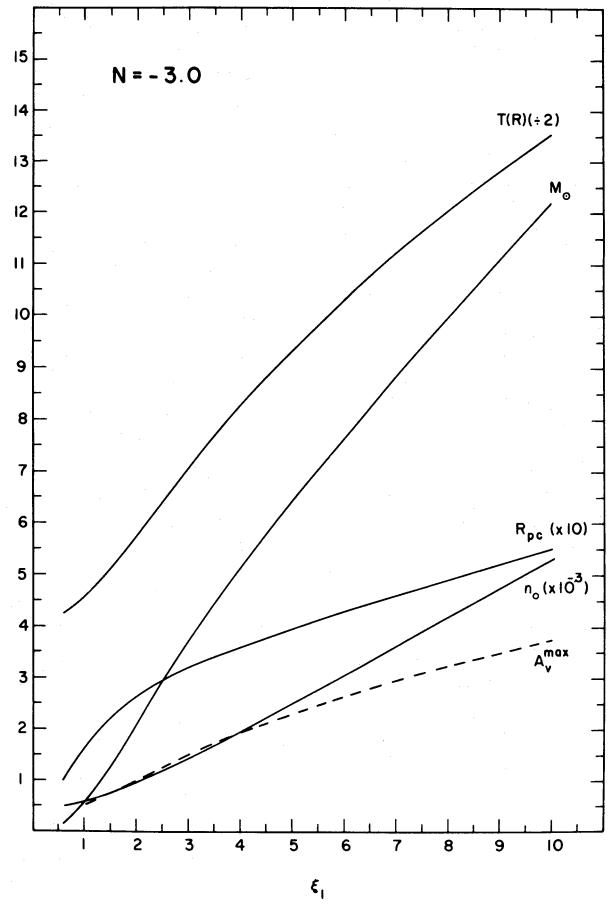

FIG. 5b

FIG. 5.—(*a*) Total mass, central H_2 number density, radius, and maximum visual extinction for a sequence of isothermal cloud models (§ IV*e*). The model temperature is 16 K, and the boundary pressure $p_0/k = 3700$ K cm^{-3} (Myers 1978). (*b*) As for Fig. 5*a*, but for a sequence of hot-edged models. The edge temperature of the models is also displayed.

It seems best to judge the quality of model fit to data primarily on the basis of the observed cloud radius and central extinction, since these are the least uncertain of the available cloud parameters. Reasonably good agreement is obtained for the isothermal models with $5 \leq \xi_1 \leq 7.5$, values which straddle the critical point $\xi_c \approx 6.4$. The total cloud mass and central H_2 number density then range from $M \approx 13.3$ to 13.7 $M_\odot$ and $n_0 \approx 3000$ to 5000 cm^{-3}, respectively. By contrast, the hot-edged model series is best fit for $7 \leq \xi_1 \leq 9$, with associated total mass, central density, and edge temperature in the ranges $M \approx 9$–11 $M_\odot$, $n_0 \approx 3500$–4700 cm^{-3}, and $T(R) \approx 22$–26 K.

From the standpoint of radius and central extinction, there is relatively little reason to prefer one class of model over the other. Both lead to cloud masses consistent with our previous estimate, and both predict central densities high enough to be qualitatively compatible with the presence of observable $C^{18}O$ emission (since this line is not strongly supported by radiative trapping). However, the hot-edged model is clearly more appealing on the physical grounds discussed previously. An additional point it its favor comes from comparing model visual extinction profiles with the equivalent A_v deduced from ^{13}CO LTE column densities (Table 2). In order to effect comparison between the spherical models and the elliptical cloud, the following approach was adopted. The position (0, 1), which marks the radio emission peak, was taken as a fiducial center about which an ellipse of axial ratio 1.3 (Table 3) was constructed. The major axis of the ellipse was aligned with that of the cloud, and the mean CO radius was used to fix the size of the ellipse via the relation $R_{CO} = (ab)^{1/2}$, where a and b are the semimajor and semiminor axes. The location of each position at which A_v was determined was then transformed into an equivalent dimensionless offset from (0, 1), specified by the ratio of the position's distance from the fiducial center to that from the center to the cloud edge along the same radial vector. Model extinction profiles were

determined by numerically integrating the hydrogen density along the appropriate sight lines and scaling by 10^{-21} (Bohlin, Savage, and Drake 1978).

Figure 6 compares the observationally based data points with the extinction profiles associated with the median best fit ξ_1 values for the isothermal and hot-edged models. The hot-edged model is clearly preferable to the isothermal one in the cloud envelope. In the center, the ^{13}CO-based extinction is considerably lower than predicted by both models (although in excellent agreement with the star count value), but the photometrically determined value, 3–5 mag, is in reasonable accord with either. The failure of the former method to faithfully trace the core extinction can be attributed to the presence of a fairly steep, unresolved ^{13}CO emission gradient in the inner portion of the cloud (§ IV*f*), which will always cause an underestimate of ^{13}CO column density (Dickman 1976).

While the hot-edged model produces a satisfactory match to the data thus far considered, it must of course be treated as a likely, rather than definitive, representation of the cloud. Other choices of p_0 and T_0 can lead to essentially the same quality of fit to the data, and the use of a polytropic equation of state is surely an oversimplification. We have, to a limited extent, explored the effect of altering our model assumptions, with the following results. Wide variations in T_0 cause the $N = -3$ models to fail; above $T_0 \approx 12$ K the equilibrium configurations are too large and massive at $\xi_1 = 8$ to be consistent with the photometric core

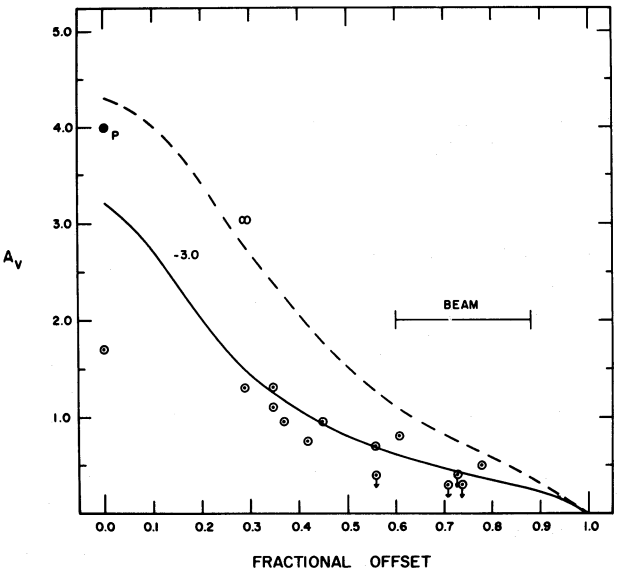

FIG. 6.—Visual extinction vs. fractional offset from cloud center for the hot-edged model with $\xi_1 = 8$ in Fig. 5*b* (*solid line*) and for the isothermal model with $\xi_1 = 7$ in Fig. 5*a* (*dashed line*). The curves were obtained by numerically integrating the local gas density along each line of sight. Also plotted are the observational results based on ^{13}CO column densities derived as in Appendix B. The point denoted "P" is based upon the surface brightness measurements and is hence unaffected by the spatial dilution effects which plague the radio-based data.

extinction, unless our distance value is in error by more than 50% (cf. Appendix A). The simultaneous imposition of R and A_v(max) as solution constraints—quantities which scale reciprocally with bounding pressure (eq. [13])—appears to restrict acceptable values of p_0 to about a $\pm 50\%$ range around Myers' (1978) value. In all cases, the hot-edged models appear superior to the isothermal ones if the admittedly uncertain equivalent A_v are compared with model extinction profiles, as in Figure 6; isothermal models which exhibit sufficiently strong density contrast to match the observed radius and core extinction and give about the correct mass and core density produce extinction profiles too steep to match the data well.

f) *Line Formation Models*

We have already remarked that the adoption of a cloud model in which the kinetic temperature increases outward renders interpretation of the spectral-line data ambiguous in some respects. For this reason, as well as to further probe the adequacy of the hot-edged models, it is useful to establish *a posteriori* that they lead to CO emission models consistent with observation.

To do so, a hot-edged polytrope with $\xi_1 = 9$ was used to establish local H_2 density and kinetic temperature throughout the model cloud; a core temperature of 8 K and a boundary pressure $p_0 = 3700\ k$ dyn cm^{-2} were assumed, so that global properties of this model can be read easily from Figure 5*b*. A Monte Carlo simulation based on that of Bernes (1979) was used for the radiative transfer. Pure microturbulence of rms amplitude $\sigma_0 = 0.12$ km s^{-1} was assumed, and the model was divided into 30 unequally spaced radial shells. Six CO rotational levels were considered, and H_2 collision rates were approximated following de Jong, Chu, and Dalgarno (1975). To obtain satisfactory convergence of the level populations, between 80 and 200 iterations for each isotopic species were typically employed. Several different random number seeds were tested to estimate the numerical noise which results from the Monte Carlo procedure (Bernes 1979). Model CO $J = 1 \rightarrow 0$ and $2 \rightarrow 1$ line intensities are accurate to better than 0.5 K; the far less saturated ^{13}CO and C^{18}O lines are considerably less noisy. Line profiles were calculated for 10 projected offsets from the model cloud center, with a velocity spacing 0.05 km s^{-1} in each profile.

In order to carry out the line formation calculations, fractional abundances of the CO isotopic species must be specified throughout the model cloud. Langer's CO chemistry (1977) was used for this purpose. For fixed hydrogen density and kinetic temperature, the CO fractional abundance, x_{CO}, is determined in Langer's computations by the UV opacity at 1000 Å, measured to the edge of his one-dimensional cloud models. Using Langer's conversion between τ_{uv} and A_v, along with integrated hydrogen densities obtained from the hydrostatic cloud model, allows one to obtain x_{CO} at each location. In the outermost portion of the model cloud, linear extrapolation of Langer's curves was used; these

regions contribute so little CO emission that virtually no error results from use of this approximation.

Langer's fractional abundances were modified in two ways. A UV flux 25% lower than Langer's was used, since the globule lies about 100 pc off the galactic plane; this flux adjustment was easily carried out by adding a constant excess τ_{uv} to each location in the cloud model. Second, Langer's models employ element depletions characteristic of the ζ Oph molecular cloud. Recent studies of carbon and oxygen depletions in interstellar clouds (Liszt 1981; de Boer 1981), however, indicate that with the exception of the upper Scorpius region, these elements are depleted by much less than 50% with respect to their solar values. CO abundances calculated with no initial gas-phase depletion therefore appear to be a more reasonable basis for the radiative transfer modeling. In order to bring them into approximate accord with a zero-depletion model, Langer's x_{CO} values were multiplied by his assumed depletion factor (however, see Mitchell, Ginsburg, and Kuntz 1978).

Langer's models account explicitly for ^{13}CO fractionation. Abundances for this species were calculated using Langer's 10 K curve, since fractionation is most pronounced in the cooler inner regions of the model cloud. Two isotope ratios $[^{12}C]/[^{13}C]$ were employed in the models: 89 (terrestrial) and 40 (Wannier *et al.* 1976). $C^{18}O$ abundance was assumed to strictly follow that of CO, scaled by two values of the $[^{16}O]/[^{18}O]$ ratio: 500 (terrestrial) and 250 (characteristic of the galactic center; Wannier 1980).

Line formation model results for the central region of the globule are given in Table 5. The line parameters summarized there have been computed by convolving the spectral-line emission for each transition and species with the response of a Gaussian antenna beam; using the adopted distance of 600 pc to the globule, the HPBW was taken to subtend either the 47″ used for the $J = 1 \rightarrow 0$ observations or the 1.′3 which was available for the $J = 2 \rightarrow 1$ data. The model results can therefore be compared directly with the observations at location (0, 1) which marks the radio peak of the actual cloud; these data are likewise listed in the Table. Radial dependences of CO and ^{13}CO $J = 1 \rightarrow 0$ radiation temperatures were also calculated and compared with the maps (Table 1), after making the geometry adjustment described in § IV*e*.

TABLE 5

MICROTURBULENT CO MODELS COMPARED WITH OBSERVATIONS

Isotopic Species	Ratio[a]	Transition $J' \rightarrow J$	Model[b] T_R	Model[b] Δv	Observed[c] T_R	Observed[c] Δv
CO.....	...	$2 \rightarrow 1$	6.8[d]	0.54	6.6	0.57
	...	$1 \rightarrow 0$	10.7	0.44	10.7	0.53
^{13}CO	1/89	$2 \rightarrow 1$	3.9	0.37	3.6	0.40
	1/89	$1 \rightarrow 0$	5.0	0.30	5.9	0.38
	1/40	$2 \rightarrow 1$	5.0	0.42	3.6	0.40
	1/40	$1 \rightarrow 0$	7.0	0.33	5.9	0.38
$C^{18}O$	1/500	$1 \rightarrow 0$	0.3	0.22	1.3	0.23
	1/250	$1 \rightarrow 0$	0.6	0.23	1.3	0.23

[a] Abundance ratio of $[^{13}C/^{12}C]$ or $[^{18}O/^{16}O]$. First values listed are solar (Allen 1973). See § IV*f*.

[b] Peak line radiation temperature (K) and FWHM (km s^{-1}) for profiles toward center of the model cloud. The tabulated results reflect convolution with synthetic antenna beams (HPBW of 47″ and 1.′3 for $1 \rightarrow 0$ and $2 \rightarrow 1$, respectively) for a cloud at 600 pc, so that results can be compared directly with observations.

[c] Peak line radiation temperature (K) and FWHM (km s^{-1}).

[d] Model line profile self-reversed. Peak does not occur at centroid velocity.

It is clear from Table 5 that the peak intensities of both modeled CO transitions agree very well with the observations. The $J = 2 \rightarrow 1$ line profile, however, is self-reversed by about 1 K in the microturbulent model, whereas the observations (Fig. 3) show only a rather flat-topped line; this discrepancy is discussed below. Considering the $\sim$0.07 km s^{-1} uncertainty attributed to our line width determinations, the full widths at half-intensity of both lines agree well with the observations. Inspection of the result for ^{13}CO shows that, within our 15%–20% calibration uncertainties, a terrestrial carbon isotope ratio produces satisfactory agreement with the observations of this species. For both CO and ^{13}CO, the synthetic $J = 1 \rightarrow 0$ maps also correspond well to the observations, and it is noteworthy that the calculated ^{13}CO brightness temperature drops very steeply past the inner 15% of the cloud radius. This steep emission gradient is responsible for the underestimate of this species' column density and hence the central extinction of the cloud discussed in the previous section.

A second exception to the generally satisfactory match between observation and theory occurs for $C^{18}O$. While the model line width agrees well with that observed—an expected agreement, since the full width at half-maximum of the $1 \rightarrow 0$ line forms the dynamical basis of the hydrostatic models (§ IV*a*)—its intensity falls substantially below the value observed, even if an oxygen isotope ratio appropriate to the galactic center is used instead of the more reasonable terrestrial value (Wannier 1980).

The two instances above in which theory and observation fail to agree are unlikely to be fatal to the present model's viability. The optically thin $C^{18}O$ line is extremely sensitive to the relatively rapid decrease in fractional abundance which the species suffers at locations even slightly displaced from the center of the model cloud. The failure of the model to account for the observed line intensity is due to the convolution of fairly strong emission from this species toward the very center of the cloud, with areas subtended by the model antenna beam which show very little $C^{18}O$ emission. This difficulty may be readily traced to our use of CO fractional abundances based upon Langer's one-dimensional cloud models: In a spherical cloud the optical depth from a given point to the cloud edge represent the *shortest* possible path for incoming radiation. In making our correspondence with Langer's calculations, we have equated just this distance to the UV path length in his one-dimensional models;

consequently, the susceptibility of CO fractional abundances to increased peripheral UV is somewhat overestimated. A full three-dimensional chemical model would be expected to lead to fractional CO abundances which decrease less steeply with radius and, consequently, to a considerably stronger $C^{18}O$ line.

Modification of Langer's published results to reflect such an alteration in cloud geometry is not trivial, especially given the anisotropic scattering properties expected for dust grains in the ultraviolet (Sherwood 1975). However, we have experimented with models which maintain $C^{18}O$ fractional abundance at its central value over about 15% of the total cloud radius and find that these can produce good agreement with the observed intensity of the line. Whether or not such a procedure is justified can, of course, be answered only by recourse to a detailed three-dimensional chemical model.

The self-reversal of the $J = 2 \rightarrow 1$ model line profile is a common attribute of microturbulent radiative transfer models for CO and is produced by optically thick CO of low excitation temperature which occults hotter material over the line formation path. The line center optical depth of the $J = 2 \rightarrow 1$ transition modeled here is about 200. For the microturbulent approximation to be valid requires the (unknown) correlation length of the random cloud motions to be smaller than $\sim 2R/200$ (Leung 1978). This is clearly a fairly stringent criterion. Recent studies of optically thick CO line formation in turbulent clouds with flow scales on the order of the photon mean free path, $\sim 2R/\tau$ (Dickman and Kleiner 1983), indicate that under such conditions self-reversals are obviated, with the emergent line profiles becoming first flat topped and then progressively more Gaussian in shape as the correlation length increases. It would therefore appear that by postulating a turbulent length scale for the globule larger than a few percent of the cloud radius, a $J = 2 \rightarrow 1$ line profile which agrees with observation could be obtained. It should also be noted that unless the correlation length is substantially larger than this value, the CO $J = 1 \rightarrow 0$ profile and those of the rarer isotopic species will be little different from those calculated via the microturbulent approximation.

V. SUMMARY AND IMPLICATIONS

We have presented a detailed radio and optical study of a compact, isolated Bok globule. The cloud lies near the extreme end of the interstellar cloud mass spectrum, having a total mass $\sim 10\ M_\odot$. The molecular lines emitted by the globule are extremely narrow, implying that turbulent motions within the cloud have an adiabatic Mach number ≤ 0.4. Consequently, thermal pressure dominates dynamical pressure within the object by at least at order of magnitude. This fact makes it relatively simple to scrutinize detailed equilibrium models for the globule, and it appears that a centrally condensed, warm-edged configuration fits the observations reasonably well. Neither the requirement of hydrostatic equilibrium nor the slight observed ellipticity of the cloud appears to demand the ad hoc postulation of a significant internal magnetic field. A best fit hydrostatic configuration was also used as the basis for a multilevel, microturbulent, non-LTE CO line formation model of the cloud. Excellent agreement was attained for ^{13}CO and $J = 1 \rightarrow 0$ CO, but a good fit could not be obtained for the $C^{18}O$ line intensity, and the CO $J = 2 \rightarrow 1$ central model profile was significantly self-reversed. The failure to account for the observed $C^{18}O$ line intensity was linked to the use of a one-dimensional chemical model to fix the fractional abundance of that species; this overestimates the effect of UV-driven destruction channels in the outer regions of a spherical cloud. It was also suggested that a line formation model embodying a flow correlation length larger than a few percent of the cloud radius might produce a better representation of the cloud's molecular emission lines.

Refinement of the crude equation of state used to model the hot-edged cloud configurations is clearly necessary before the future evolution of the globule can be seriously explored. While it is unlikely that an improved equation of state will possess the simple analytic properties of a polytrope, it would not be surprising to find a Bonnor-type instability allowed at sufficiently high values of the boundary pressure, given a more realistic pressure-density relation for the cloud. The near-term fate of the globule would then depend strongly upon the present velocity of the cloud with respect to the galactic plane, since higher ambient pressures may be expected there. Other possible evolutionary scenarios for the object include either assimilation of the globule by collision with a larger molecular (or atomic) cloud or evaporation into the intercloud medium. The former is of relatively high likelihood if the cloud possesses a significant velocity component back toward the galactic plane. The latter process depends strongly on the nature of the surrounding medium. If embedded in coronal gas at $T \sim 10^6$ K, the cloud will evaporate in only 50 million years or so (Cowie and McKee 1977). On the other hand, if the globule is buffered by cooler and denser H I for which $T \leq 10^4$ K (Spitzer 1978), its evaporation time will be greatly lengthened.

The most striking aspect of this study is the finding that any turbulent motions within the globule are subsonic. This afforded an opportunity to study a self-gravitating system freed of many of the ambiguities usually associated with stochastic hydrodynamic states. The physical isolation of the cloud is essential in this respect; the situation would be far more complex if the cloud were embedded in a dense, turbulent medium of comparable kinetic temperature. In that case, the occurrence of density fluctuations whose lifetimes are prolonged by self-gravity would be an expected consequence of the compressibility of the gas. The stability of such condensations can only be judged by recourse to a full hydrodynamic treatment of both the turbulent condensation *and* its embedding material.

The role of turbulence in supporting molecular clouds is presently a topic of considerable debate (e.g., Scalo

and Pumphrey 1982). An important feature of subsonic stochastic flows is that they are somewhat more amenable to detailed theoretical study than their supersonic counterparts (e.g., Sasao 1973). If a set of objects similar to the present cloud could be studied at sufficiently high spatial resolution, an *observational* framework capable of supporting theoretical work on compressible turbulence through the poorly understood sonic transition may be possible. Based on optical morphology alone, we suspect that such clouds may be common: compact, regular, bright-rimmed clouds such as the Thumbprint Nebula in Chamaeleon and the chain of globules near $\alpha = 20^{h}48^{m}, \delta = 66°$ are but a few examples.

We are pleased to acknowledge useful discussions with Drs. Tom Arny, David Black, Paul Goldsmith, Ted Harrison, Jocelyn Keene, Phil Myers, Frank Shu, and Karen Villere on various aspects of this work. We are grateful to Dr. Helmut Abt and Mr. Glynn Pickens of Kitt Peak National Observatory for obtaining the POSS photograph of the globule shown in Figure 1. This study was supported by the National Science Foundation under grant AST 81-21481 to Five College Radio Astronomy Observatory. This is contribution number 526 of the Five College Astronomy Department.

APPENDIX A

DISTANCE TO THE GLOBULE

Four techniques were utilized to estimate the globule's distance, d. Using the Schmidt (1965) model together with the cloud's galactic coordinates and observed radial velocity leads to a kinematic distance (e.g., Lang 1974)

$$d_{\rm kin} = 900\ (\pm 400)\ {\rm pc}\ , \tag{A1}$$

assuming the Oort constant $A = 15$ km s^{-1} kpc^{-1}. The uncertainty given above is based solely upon a ± 5 km s^{-1} random cloud velocity along the line of sight (Sanders 1982). The failure of the Schmidt model beyond the solar circle (e.g., Roberts 1972) and/or the presence of a significant noncircular velocity component imparted to the globule in its formation are additional, potential systematic errors in equation (A1).

Recent large-scale CO surveys of the Milky Way suggest a molecular cloud scale height ~ 85 pc in the second quadrant, with some hint that this depends inversely upon cloud mass (D. Sanders, private communication). Assuming the globule to lie within two scale heights of the galactic plane then yields an upper limit to its distance, using $b = -10°$, of

$$d_z \leq 980\ {\rm pc}\ . \tag{A2}$$

Herbst and Sawyer (1981) recently recalibrated a distance estimation scheme for dark nebulae originally due to Bok (e.g., Bok and McCarthy 1974). The technique is based upon the fact that the farther away an interstellar cloud is, the larger the number of interposed foreground stars will be. Herbst and Sawyer find that the distance to a completely opaque cloud of surface area a is related to the number of foreground stars seen on the blue POSS print, n_0, via

$$d_F = 320[n_0(a_5/a)]^{0.57}\ {\rm pc}\ , \tag{A3}$$

where a_5 is the area of a 5′ diameter circle.

Although the globule core is indeed opaque on the blue POSS print (but not on the red; cf. § III), its area is too small to yield a meaningful distance. However, we have previously noted that the L1295 complex lies $\sim 1°$ from the globule and possesses a radial velocity less than 0.5 km s^{-1} different from the latter. Given the extreme isolation of both clouds, it seems reasonable to attribute a common distance to them. Visual inspection of L1295 on the POSS O print revealed at least nine stars judged to be probable foreground objects. Using the measured value $(a_5/a) \approx 0.36$ for the simply connected region searched then yields, using relation (A3),

$$d_F({\rm L1295}) \approx 625^{+110}_{-130}\ {\rm pc}\ , \tag{A4}$$

where the uncertainty is due only to counting statistics.

Another technique for estimating distances to dark nebulae is described by Snell (1979, 1981). The method exploits the fact that statistically, dark clouds appear to be segregated into more or less discrete layers with respect to distance from the Sun (see Lynds 1968 for review); although the visual opacity in a given layer may exhibit large fluctuations with position, layers can usually be traced over many square degrees. Given MK spectral types, visual magnitudes, and measured $(B-V)$ colors for an ensemble of stars in the vicinity of a cloud, one can ascertain for each star the color excess E_{B-V} and distance, based upon the intrinsic color $(B-V)_0$ and absolute magnitude associated with its spectral type and luminosity class. A plot of E_{B-V} versus distance for stars in the vicinity of a particular cloud can then be expected to show "steps" at one or more discrete distances, each step being associated with an intervening cloud layer.

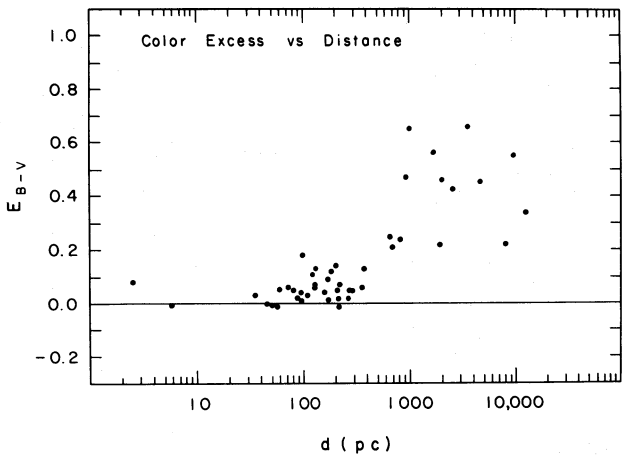

FIG. 7.—Color excess vs. distance for stars in the vicinity of the globule. The selection criteria described in Appendix A were imposed on the sample in order to inhibit confusion by relatively nearby sheets of obscuring material which lie closer to the galactic plane than the globule. The discontinuity in color excess at about 700 pc marks the appearance of a layer of absorbing matter at, or somewhat closer than, this distance.

There are two drawbacks to this technique. First, very large areas (Snell used 20° × 20°) must be employed because MK spectral data and colors are available for a rather limited number of stars. Second, if several layers of absorbing material are revealed by the analysis, to which (if any) does the cloud belong? This second issue is particularly acute in the present case. The large-scale extinction *in* and *above* the galactic plane in the vicinity of the globule has been studied by several workers (Baker and Nantkes 1944; Nantkes and Baker 1948; Heeschen 1951). All three investigations found at least two extended absorbing sheets, one at 300–500 pc from the Sun, the other at about 800 pc. Because the foregoing distance estimates are compatible with much greater values than 300 pc, it is clear that if the closer layer does not extend to the depressed latitude of the globule ($b \sim -10°$), the inclusion of stars with $0° \leq b \leq 10°$ will needlessly add confusion to the color excess versus distance correlation desired here.

The color excess method was therefore applied only to stars in the range $0^h3^m \leq \alpha \leq 1^h10^m$, $60° \leq \delta \leq 44°$, corresponding to a region approximately 11° × 16° in size; the declination cutoff at ~60° ensures that only stars at $b \leq -3°$ are included in the sample. Some 50 stars in this range for which spectral and color data are available were found in the catalog of Kennedy and Buscombe (1974). Absolute magnitudes and intrinsic colors based upon the tabulated spectral and luminosity classes were then obtained from the compilation of Schmidt-Kaler (1967). The resulting E_{B-V} versus log d plot is shown in Figure 7. The presence of an absorbing layer at $d \leq 600$–700 pc is clearly evident.

We therefore find a rough upper limit to the globule's distance based upon the color excess method of

$$d_{CE} \leq 700 \text{ pc} . \tag{A5}$$

This value represents an upper limit because the sample of stars used in its derivation is too small to allow a more precise location of the color excess discontinuity in the E_{B-V} versus d plot.

Of the four methods considered, only two—the foreground star and color excess approaches—provide results refined enough to warrant use; the scale height and kinematic methods are, however, in accord with the other two. Taken together, the foreground star and color excess approaches suggest $d \sim 500$–700 pc. We therefore adopt 600 pc as the distance to the globule.

APPENDIX B

^{13}CO-A_v RELATION

Here a method is developed to extract equivalent visual extinctions at each location in the globule where ^{13}CO LTE column densities were obtained. The starting point is the correlation between these two quantities found by Dickman (1978*b*) for a large sample of dark clouds. As pointed out by J. Keene (private communication), a more

accurate CO dipole moment than that used by Dickman is available (0.11 versus 0.1 debye). This leads to a slightly smaller (by $\sim 25\%$) slope for the A_v-N_{13} relation:[3]

$$A_v = 0.52[N_{13}(\mathrm{LTE})/10^{15}\ \mathrm{cm}^{-2}]\ \mathrm{mag}\ . \tag{B1}$$

The maximum extinction for the globule obtained in this way, 1.7 mag at (0, 1), is in excellent agreement with the average core extinction of 1.85 mag deduced from the star counts (§ III*b*). This strongly suggests that the ^{13}CO-A_v relation toward the central regions of the globule is typical of the sample studied by Dickman. It would be inappropriate, however, to apply relation (B1) to the $\geq 50\%$ of the globule area for which $A_v \leq 1.5$ mag, that is, for which $N_{13} \leq 2.9 \times 10^{15}$ cm^{-2}. This regime was not adequately sampled by Dickman, and it is expected that the decreasing fractional abundance of CO in the cloud envelope will lead to extinction underestimates if equation (B1) is used.

To characterize the cloud envelope, we shall assume a quadratic relation between N_{13} and A_v of the form

$$N_{13} = \gamma A_v^2 \qquad \text{for} \qquad A_v \leq 1.5\ , \tag{B2}$$

where γ is to be determined. Federman *et al.* (1980) have found a relation of this kind to apply in diffuse clouds between CO column density and extinction (if a standard gas-to-extinction ratio is used). Although in general CO and ^{13}CO abundances are not proportional, owing to the action of isotopic fractionation (Watson, Anicich, and Huntress 1976), they are approximately so in the interval of interest here, $0.1 \leq A_v \leq 1.5$ (see especially Table 3 of Federman *et al.*).

To fix the constant γ, we impose the requirement that both equations (B1) and (B2) yield the same column density at $A_v = 1.5$, so that $\gamma \approx 1.3 \times 10^{15}$ cm^{-2} mag^{-2}. This approach seems preferable to directly scaling Federman *et al.*'s proportionality constant by their calculated (and highly fractionated) $\sim 30{:}1$ isotope ratio, for two reasons. First, it requires only a generic similarity between the globule envelope and the diffuse clouds studied by Federman *et al.*; the globule envelope may in fact be denser and cooler than typical diffuse clouds (cf. § IV*e*). Second, it ensures continuity between the *assumed* behavior in the low-opacity regime and the *observed* ^{13}CO-A_v correlation at larger extinctions. We note that if one instead assumes Federman *et al.*'s coefficient, corrected for fractionation, to apply, agreement with relation (B1) is attained at $A_v \approx 3$ mag. This value is so high that the agreement between the core-averaged extinction from the star counts and that derived using equation (B1) would have to be regarded as fortuitous.

[3] For *direct* conversions of N_{13}(LTE) to equivalent molecular hydrogen column densities, Dickman's (1978*b*) result $N_{H_2} \approx 5 \times 10^5 N_{13}$(LTE) may be used without significant modification. This is because the earlier work employed $N_{H_2}/A_v = 1.25 \times 10^{21}$ cm^{-2} mag^{-1} (Jenkins and Savage 1974), a value about 1.25 times larger than the most recent determination (Bohlin, Savage, and Drake 1978). The revision in the gas-to-extinction ratio almost exactly compensates for the error resulting from use of the imprecise CO dipole moment.

REFERENCES

Allen, C. W. 1973, *Astrophysical Quantities* (3d ed.; London: Athlone).
Baker, R. H., and Nantkes, E. 1944, *Ap. J.*, **99**, 125.
Bernes, C. 1979, *Astr. Ap.*, **73**, 67.
Bohlin, R. C., Savage, B. D., and Drake, J. F. 1978, *Ap. J.*, **224**, 132.
Bok, B. J. 1956, *A.J.*, **61**, 309.
Bok, B. J., and McCarthy, C. C. 1974, *A.J.*, **79**, 42.
Bonnor, W. B. 1956, *M.N.R.A.S.*, **116**, 351.
———. 1958, *M.N.R.A.S.*, **118**, 523.
Chandrasekhar, S. 1939, *An Introduction to the Study of Stellar Structure* (New York: Dover).
Cowie, L. L., and McKee, C. F. 1977, *Ap. J.*, **211**, 135.
Cox, D. P. 1979, *Ap. J.*, **234**, 863.
de Boer, K. S. 1981, *Ap. J.*, **244**, 848.
de Jong, T., Chu, S. I., and Dalgarno, A. 1975, *Ap. J.*, **199**, 69.
de Jong, T., Dalgarno, A., and Boland, W. 1980, *Astr. Ap.*, **91**, 68.
Dickman, R. L. 1976, Ph.D. thesis, Columbia University.
———. 1978*a*, *A.J.*, **83**, 363.
———. 1978*b*, *Ap. J. Suppl.*, **37**, 407.
Dickman, R., and Kleiner, S. 1983, in preparation.
Dickman, R. L., McCutcheon, W. H., and Shuter, W. L. H. 1979, *Ap. J.*, **234**, 100.
Dyson, J. E. 1973, *Astr. Ap.*, **27**, 459.
Erickson, N. 1981, *IEEE Trans.*, **MTT-29**, 557.
Federman, S. R., Glassgold, A. E., Jenkins, E. B., and Shaya, E. J. 1980, *Ap. J.*, **242**, 545.
FitzGerald, M. P., Stephens, T. C., and Witt, A. N. 1976, *Ap. J.*, **208**, 709 (FSW).
Goldsmith, P. F., and Langer, W. D. 1978, *Ap. J.*, **222**, 881.
Heeschen, D. S. 1951, *Ap. J.*, **114**, 132.
Herbst, W., and Sawyer, D. 1981, *Ap. J.*, **243**. 935.
Jenkins, E. B., and Savage, B. D. 1974, *Ap. J.*, **187**, 243.
Kennedy, P. M., and Buscombe, W. 1974, *MK Spectral Classifications* (Evanston, Ill.: Northwestern University).
Kimura, H. 1981, *Pub. Astr. Soc. Japan*, **33**, 299.
Kutner, M. L., and Ulich, B. L. 1981, *Ap. J.*, **250**, 341.
Lang, K. R. 1974, *Astrophysical Formulae* (Berlin: Springer-Verlag).
Langer, W. D. 1977, *Ap. J.* (*Letters*), **212**, L39.
Leung, C. M. 1978, *Ap. J.*, **225**, 427.
Liszt, H. S. 1981, *Ap. J.* (*Letters*), **246**, L147.
Lynds, B. T. 1968, in *Stars and Stellar Systems*, Vol. **7**, *Nebulae and Interstellar Matter*, ed. B. M. Middlehurst and L. H. Aller (Chicago: University of Chicago Press).
Matilla, K. 1970*a*, *Astr. Ap.*, **8**, 273.
———. 1970*b*, *Astr. Ap.*, **9**, 53.
Milne, A. E. 1930, *Handbuch der Astrophysik*, Vol. **3**, Pt. 1, p. 63. (Reprinted in D. H. Mestel, ed. 1966, *Selected Papers on the Transfer of Radiation* [New York: Dover].)
Mitchell, G. F., Ginsburg, J. L., and Kuntz, P. J. 1978, *Ap. J. Suppl.*, **38**, 39.
Mouschovias, T. Ch. 1976, *Ap. J.*, **206**, 753.
Myers, P. C. 1978, *Ap. J.*, **225**, 380.
Myers, P. J., and Benson, P. J. 1982, *Bull. AAS*, **14**, 642.
Nantkes, E., and Baker, R. H. 1948, *Ap. J.*, **107**, 113.
Penzias, A. A., and Burrus, C. A. 1973, *Ann. Rev. Astr. Ap.*, **11**, 51.
Roach, F. E. 1967, in *Modern Astrophysics: A Memorial to Otto Struve*, ed. M. Hack (Paris: Gauthier-Villars), p. 49.
Roberts, W. W. 1972, *Ap. J.*, **173**, 259.

Sanders, D. B. 1982, Ph.D. thesis, State University of New York.
Sasao, T. 1973, *Pub. Astr. Soc. Japan*, **25**, 1.
Scalo, J. M., and Pumphrey, W. A. 1982, *Ap. J.* (*Letters*), **258**, L29.
Schmidt, E. G. 1975, *M.N.R.A.S.*, **172**, 401.
Schmidt, M. 1965, in *Stars and Stellar Systems*, Vol. **5**, *Galactic Structure*, ed. A. Blaauw and M. Schmidt (Chicago: University of Chicago Press).
Schmidt-Kaler, Th. 1967, *IAU Symposium 31, Radio Astronomy and the Galactic System*, ed. H. van Woerden (London: Academic).
Sherwood, W. A. 1975, *Ap. Space Sci.*, **34**, 1.
Shu, F. H., Milione, V., Gebel, W., Yuan, C., Goldsmith, D. W., and Roberts, W. W. 1972, *Ap. J.*, **173**, 557.
Snell, R. L. 1979, Ph.D. thesis, University of Texas.
———. 1981, *Ap. J. Suppl.*, **45**, 121.
Spitzer, L. 1968, in *Stars and Stellar Systems*, Vol. **7**, *Nebulae and Interstellar Matter*, ed. B. M. Middlehurst and L. H. Aller (Chicago: University of Chicago Press), p. 1.
Spitzer, L. 1978, *Physical Processes in the Interstellar Medium* (New York: Wiley).
———. 1982, *Ap. J.*, **262**, 315.
Traving, G. 1975, in *Problems in Stellar Atmospheres and Envelopes* (New York: Springer-Verlag), p. 325.
Viala, Y., and Horedt, G. P. 1974, *Astr. Ap. Suppl.*, **16**, 173.
Wannier, P. G. 1980, *Ann. Rev. Astr. Ap.*, **18**, 399.
Wannier, P. G., Penzias, A. A., Linke, R. A., and Wilson, R. W. 1976, *Ap. J.*, **204**, 26.
Watson, W. D., Anicich, V. G., and Huntress, W. T. 1976, *Ap. J.* (*Letters*), **205**, L165.
Witt, A. N. 1968, *Nature*, **220**, 50.
Witt, A. N., and Stephens, T. C. 1974, *A.J.*, **79**, 948 (WS).

DAN P. CLEMENS and R. L. DICKMAN: Radio Astronomy, GRC, University of Massachusetts, Amherst, MA 01003

1983ApJ...271..143D

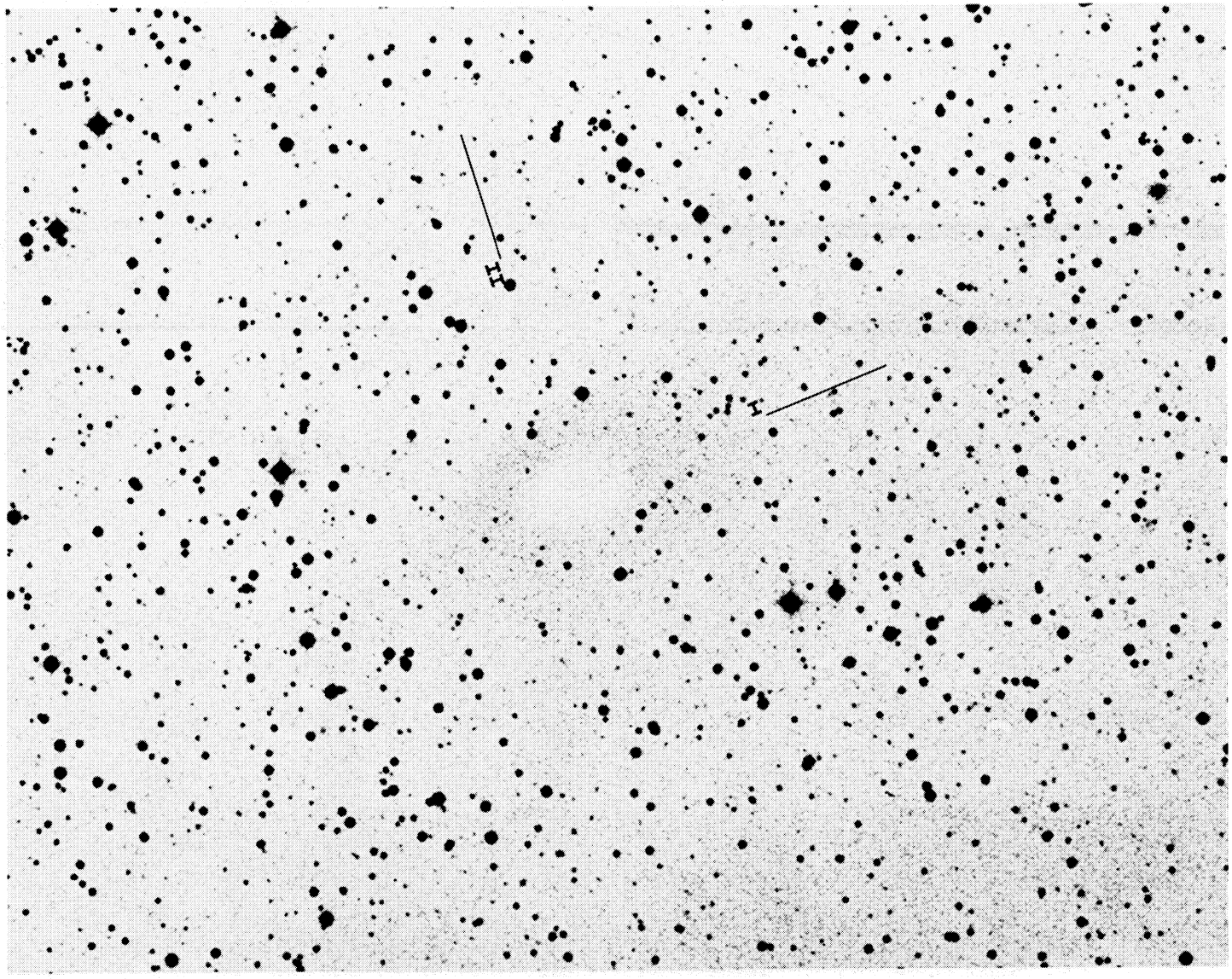

FIG. 1.—Enlargement of POSS O print showing the globule. Approximate central coordinates are $\alpha(1950) = 0^h36^m17^s.0$, $\delta(1950) = 52°34'37''$ (§ III*a*). Note the opaque inner core and bright diffuse rim. The cross marks above the globule image are 2′ in length and denote the major and minor axis directions for the densitometric tracings in Fig. 2.